Design and performance of the *Astro-E*/XRS microcalorimeter array and anti-coincidence detector

C. K. Stahle[*a], M. D. Audley[a,b], K. R. Boyce[a], R. P. Brekosky[a,c], R. Fujimoto[d], K. C. Gendreau[a,b], J. D. Gygax[a,c], Y. Ishisaki[e], R. L. Kelley[a], R. A. McClanahan[a], T. Mihara[f], K. Mitsuda[d], S. H. Moseley[a], D. B. Mott[a], F. S. Porter[a], C. M. Stahle[a], A. E. Szymkowiak[a]

[a]NASA /Goddard Space Flight Center, Greenbelt, MD 20771 USA
[b]Department of Astronomy, University of Maryland, USA
[c]Swales Corporation, USA
[d]Institute of Space and Astronautical Science (ISAS), Japan
[e]Tokyo Metropolitan University, Japan
[f]The Institute of Physical and Chemical Research (RIKEN), Japan

ABSTRACT

The XRS instrument has an array of 32 micro-calorimeters at the focal plane. These calorimeters consist of ion-implanted silicon thermistors and HgTe thermalizing x-ray absorbers. These devices have demonstrated a resolution of 9 eV at 3 keV and 11 eV at 6 keV. We will discuss the basic physical parameters of this array, including the array layout, thermal conductance of the link to the heat sink, operating temperature, thermistor size, absorber choice, and means of attaching the absorber to the thermistor bearing element. We will present representative performance data, though a more detailed presentation of the results of the instrument calibration is presented elsewhere in these proceedings. A silicon ionization detector is located behind the calorimeter array and serves to reject events due to cosmic rays. We will briefly describe this anti-coincidence detector and its performance in conjunction with the array.

Keywords: XRS, Astro-E, microcalorimeter, spectroscopy, x-ray

1. INTRODUCTION

The XRS (X-Ray Spectrometer)[1], a microcalorimeter array and anti-coincidence detector at the focus of conical foil X-ray optics, is one of the instruments aboard *Astro-E*[2], a Japanese x-ray astronomy satellite to be launched early in the year 2000. Its 32-pixel array will cover 7.8 square arc-minutes of the focal plane, providing 8–14 eV resolution across the band from 0.3–14 keV. XRS will open the field of high-throughput, high-resolution astrophysical x-ray spectroscopy, which will be a powerful tool for the study of astronomical plasmas.

Since celestial x-ray sources typically have low fluxes, a useful spectrometer must be efficient in addition to having high spectral resolution. The invention of microcalorimeters was motivated by shortcomings in both dispersive and non-dispersive x-ray spectrometers. Dispersive spectrometers, such as gratings, offer extremely high energy resolution, particularly at low energies, but can have low quantum efficiency and may not be suitable for the study of extended sources. Non-dispersive spectrometers based on ionization in silicon, such as diodes and charge-coupled devices, have higher quantum efficiency but lower energy resolution due to the statistics of charge production and collection in silicon. Microcalorimeters, which are solid state detectors based on the measurement of heat instead of charge, allow both high efficiency and high resolution.

Because a fraction of cosmic rays that traverse the calorimeter pixels will leave behind energy comparable to photons in the XRS spectral bandwidth, an anti-coincidence detector was implemented both to reject cosmic ray events and to be a rapidly responding witness of the particle environment. The original design for the anti-coincidence detector was for it to be a

* Correspondence: Email: Caroline.Stahle@gsfc.nasa.gov

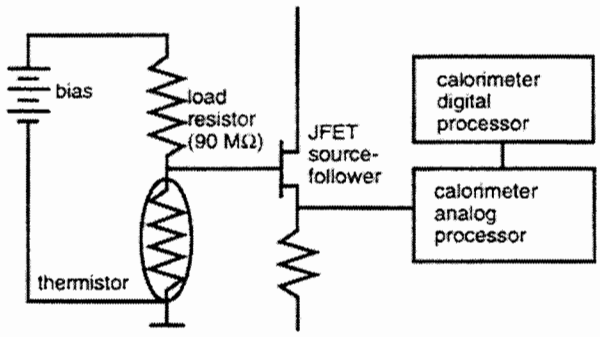

Figure 1: Block diagram of the XRS calorimeter bias circuit and signal processing for a single channel.

calorimeter also, albeit a bigger, slower, and more poorly resolving one than the pixels in the array. It was replaced with a silicon ionization detector in order to provide a faster signal with temperature invariant gain.

2. PHYSICAL DESCRIPTION OF THE XRS ARRAY

An x-ray calorimeter is a conceptually simple device. It consists of a low-heat-capacity mass to absorb and thermalize incident x-ray photons, a weak link to a low-temperature (< 0.1 K) heat sink that provides the thermal isolation needed for a temperature rise to occur, and a thermometer to measure that change in temperature. The specific implementation of the basic calorimeter concept in XRS uses ion-implanted silicon thermistors and HgTe X-ray absorbers. Thin silicon beams form the weak links to a 60 mK heat sink. Each device in the array is current-biased through a 90 MΩ load resistor, and the change in the voltage dropped across the thermistor as its resistance changes is the x-ray signal. As shown in Figure 1, the signal is passed through a Junction Field Effect Transistor (JFET) source-follower (operated at a temperature of 120 – 130 K) to lower the output impedance on its way to amplification in the Calorimeter Analog Processor (CAP) and signal processing in the Calorimeter Digital Processor (CDP). The CDP[3] calculates and applies the optimal digital filter[4] needed to obtain the highest energy resolution and, in standard operation, telemeters the pulse height, rise time, trigger time, and quality flags (including the anti-coincidence flag) for each triggering pulse.

2.1. Array Geometry

The area of an individual detector element is determined by heat capacity constraints placed on the absorber, the thickness of which is dictated by the required efficiency. The number of pixels is limited by the complexity of the readout electronics. Balancing focal plane coverage, complexity, efficiency, and resolution, the final XRS array design has 32 elements of 0.39 mm^2 area each in a 2×18 bilinear layout. (In the instrument, the corner four pixels are unused.) Each array is formed monolithically from silicon (except for the absorber attachment) using photo-lithographic processes.[5] The final thickness of the suspended elements and their support beams is 14-15 μm, while the heat sinking frame remains 350 μm, the initial thickness of the silicon wafer. Each suspended element is 1.0 mm × 0.25 mm and is supported by three silicon beams, with the third beam running between two pixels in the other row. Each oversized absorber (1.23 mm × 0.32 mm) covers the third beam to the right of the pixel on which it is placed. The thermistors are formed by ion-implanted phosphorus with 50% boron compensation. Contact leads are made by degenerately doping with phosphorus. Beam blockers made of 300 μm thick silicon cover the exposed thermal links to reduce the number of x-rays being absorbed there. Figures 2 and 3 show a complete and a close-up view of the array. (The figures are from Reference 6). All of the detector fabrication, with the exception of the growth of the absorber material, was performed at Goddard Space Flight Center, in the laboratories of the Detector Systems Branch and the X-ray Astrophysics Branch.

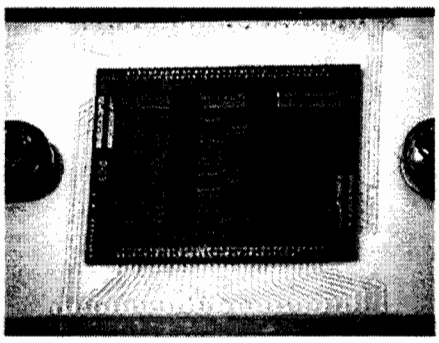

Figure 2: XRS-style bilinear array

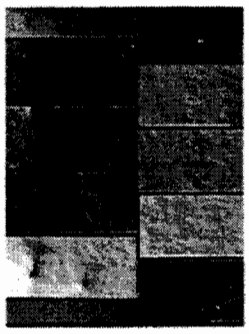

Figure 3: Close-up of XRS array

2.2. X-ray Absorbers

The X-ray absorbers used in XRS are 8.5 μm thick pieces of HgTe. HgTe is used, despite a relatively low Debye temperature (140 K), because of the high atomic numbers of its constituents and because of its demonstrated good thermalization of x-rays. The HgTe was grown by molecular beam epitaxy on CdZnTe substrates by Texas Instruments, and the substrate material was removed at Goddard. We reduce position-dependent variations in the signal by controlling the extent and thermal conductance of the link between the absorber and thermistor.[7,8] We affix a spacer (a 12 μm × 0.24 mm × 0.24 mm piece of silicon) to each suspended thermistor element and then attach the absorber to the spacer. Both adhesive joints are made of Stycast 1266, and we aim for a ~25 μm diameter sphere of epoxy prior to application at each interface. The spacer confines the epoxy, which otherwise could wick between the flat surfaces of the absorber and pixel. The spacer also raises the absorbers above the plane of the monolithic array, avoiding contact between the absorbers and the other parts of the array structure that they overhang.

2.3. The Thermistor and Weak Link

We needed to optimize simultaneously the size and shape of the thermistor, the thermal conductance of the link to the heat sink, and the thermistor resistance and its derivative with temperature (R and dR/dT) at the operating point. Issues considered included excess noise, heat capacity, and non-ohmic behavior. Conduction in a doped semiconductor at low temperatures proceeds via Variable Range Hopping (VRH), by which localized electrons hop by phonon-assisted tunneling between isolated impurity energy levels. As the temperature is lowered, the average hopping length increases because there are few nearby sites with energy levels accessible by thermal excitation. In the case of a Coulomb gap,[9] resistance should follow $R = R_0 \exp\left(\sqrt{T_0/T}\right)$. The temperature is T, and one controls T_0 with the dopant concentration and R_0 with the aspect ratio. We want the magnitude of the resistance to be well-matched to the silicon JFET pre-amplifiers, which restricts the value to be ~ 10 MΩ, and certainly no greater than 90 MΩ, the value of the load resistor. To have a large value of T_0, yet keep the resistance under these limits, would require a thermistor with width much greater than the distance between the contacts. This would come with the penalty of the excess heat capacity associated with the degenerately doped regions used to make these wide contacts, even if there were no non-ideal behavior associated with large values of T_0. We used thermistor areas of 200 μm × 200 μm and 200 μm × 400 μm in variations of the bilinear design. The implant depth (the extent of the flat part of the density profile) is nominally 0.3 μm.

We used a ^{3}He refrigerator to screen test devices from our device runs. Our devices follow the expected VRH resistance function very well from 1.5 K to 0.3 K, from which we determined values for R_0 and T_0, but these underestimated the actual resistance at our operating point near 65 mK. Such deviation has been observed by Zhang, et al.[10] in similar thermistors. A possible origin of the increase in resistance is the onset of thickness dependence due to truncation of the network of accessible energy levels. Whatever the mechanism, we found we needed a lower T_0 (as determined over the range 0.3 to 1 K) than expected to obtain a particular resistance at the operating temperature.

Another limit on the value of T_0 is 1/f noise from resistance fluctuations (dR/R) in our thermistors. This noise increases with T_0. During the development of the XRS devices, we did not examine enough different values of T_0 to determine the precise dependence nor to understand the impact of the resistance enhancement at low temperatures on the noise. It was clear from our spectral results, though, that resolution did not improve with values of T_0 greater than about 6 K, so we defined our range of acceptable values to be 5 - 6 K. Recently Han et al.[11] parameterized this excess noise in terms of the electron temperature as determined in a hot-electron model, the area of the thermistor, and T_0, for an implant depth comparable to that used in XRS. Experiments to determine the dependence of the noise on implant depth have not yet been conducted.

The value of the thermal conductance of the link to the heat sink is also set by non-ideal effects. Our devices exhibit non-ohmic behavior consistent with a hot-electron model as parameterized by Zhang, et al.[12] In an ideal calorimeter with a resistive thermometer, the signal-to-noise ratio improves with increases in bias until self-heating diminishes the responsivity. This effect results in an optimum bias temperature independent of the thermal conductance. Non-ohmic behavior appears as a thermal impedance between the electrons of the thermometer and the crystal lattice. As the thermal conductance of the weak link approaches that of this link between the electrons and the lattice, the device will begin to lose responsivity at biases less than the nominal optimum. The upper limit on the thermal conductance of the weak link depends on the thermistor area and T_0. Count rate considerations and sensitivity to stray background power limit how low we are willing to make this

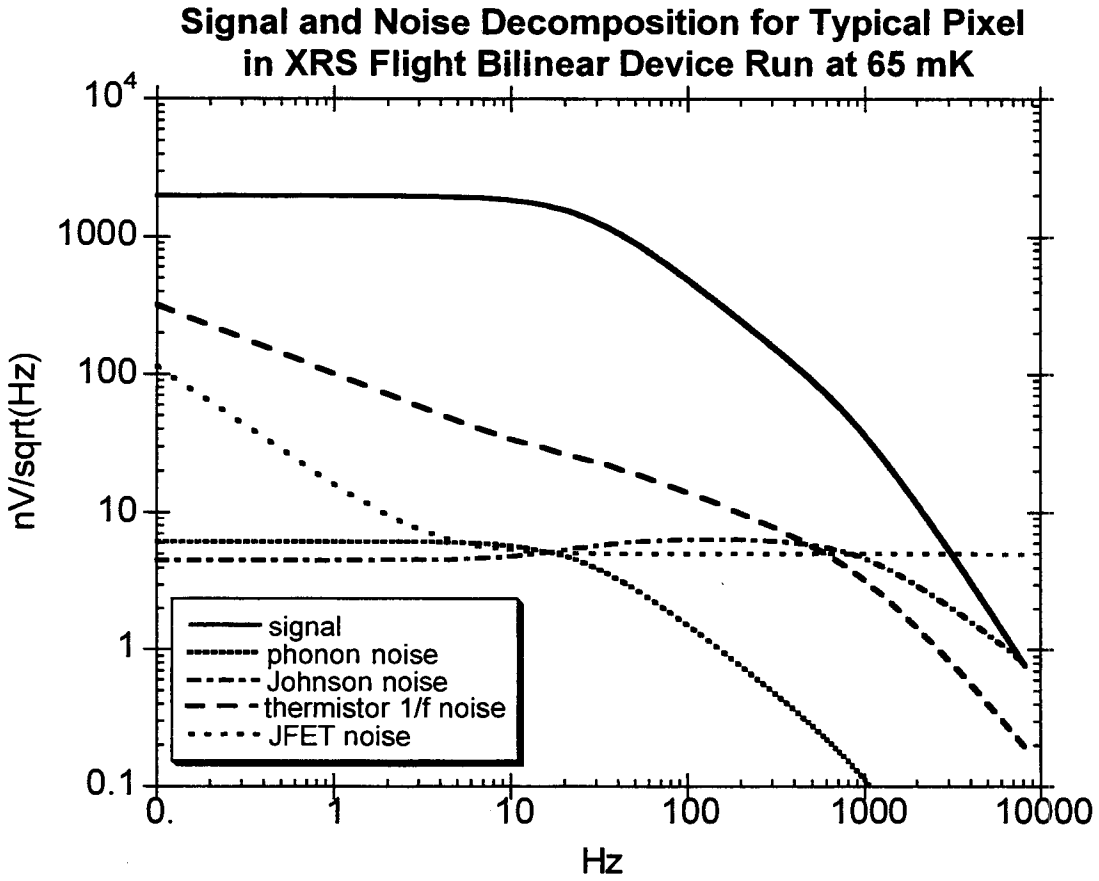

Figure 4. The signal and the computed components of the noise from a pixel in the XRS bilinear array operated in the laboratory test apparatus with a 65 mK heat sink temperature.

thermal conductance. The optimum for the XRS-style devices is a value for the thermal conductance in the range $3 - 4.5 \times 10^{-11}$ $(T/0.1)^3$ W/K. The flight array, with 200 μm × 400 μm thermistors, works well at 4.0×10^{-11} $(T/0.1)^3$ W/K. The thermal conductance is controlled through the thickness of the silicon beams and through the texturing of the back surface with a chemical etch to make the phonon transport down the beams less specular and more diffusive. Variation in the degree of roughness has been the primary source of differences in thermal conductance between processed lots.

XRS was designed around a 65 mK base temperature, supplied by an adiabatic demagnetization refrigerator (ADR). Operating temperature is traded against mission lifetime and the acceptable ADR duty cycle (operating time versus recharge time), otherwise we would want to design the calorimeters for the lowest possible heat sink temperature in order to obtain the highest resolution. The XRS ADR[13] is performing above requirements, so recently the base operating temperature has been changed to 60 mK.

3. EXPECTED AND MEASURED PERFORMANCE OF THE XRS ARRAY

In the end we produced several runs of arrays with similar resolution and pulse recovery times. A majority of theses devices exhibited resolution of 8 - 9 eV (FWHM) at the baseline, 9 - 10 eV at 3.3 keV, and 11 - 12 eV at 5.9 keV when digitized data were processed with an optimal digital filter. The baseline contribution is determined by using the relationship between filtered pulse height and energy to express the noise level in the absence of x-rays in terms of energy. The increase in line width with energy is due to pulse height non-linearity. On some devices we have seen additional degradation in the resolution with energy, which acts as an additional noise term that scales linearly with the photon energy and adds in quadrature with the baseline noise. Summing the contributions to the heat capacity, including an excess sometimes needed to explain the pulse shapes, the Moseley, Mather and McCammon resolution expression[14] predicts a baseline resolution of 3 eV. This calculation assumes the noise is dominated by phonon noise (due to thermal fluctuations across the weak link) and Johnson noise. Figure 4 shows the signal and a computed decomposition of the noise as a function of frequency for a device

in an array operated with a 65 mK heat sink in a dilution refrigerator test apparatus. This array eventually was designated the flight array. All the curves except the JFET voltage noise include the roll-off due to the RC low pass filter formed by the thermistor resistance and parasitic capacitance between the JFET gate and ground. The Johnson noise and thermometer excess noise curves include the effect of electrothermal feedback, which suppresses them at frequencies below the knee in the signal curve. (Electrothermal feedback is the result of the change in Joule power that accompanies a change in the thermistor resistance.) The effects of the signal AC coupling and the anti-aliasing filter were not included as these would be applied to all the curves without changing their relative values. The excess noise and JFET noise are based on measured values, with the JFET represented here being among the noisier of the XRS flight JFETs. The Johnson noise and phonon noise were calculated from measured detector parameters.[15,16] The total noise is clearly dominated by the thermistor 1/f noise. This plot graphically shows at least one reason why the 3 eV resolution predicted in the absence of excess noise is not obtained. Nevertheless, the design goal for XRS was to obtain better than 12 eV resolution, and having done so represents a major advance for x-ray astronomy.

Calibration of XRS was performed primarily at a heat sink of 60 mK. The array showed excellent uniformity, with less than 13% variation in resolution across the pixels. The FWHM resolution at 3 keV was 9-10 eV and at 6 keV was 11-12 eV. Figure 5 shows a representative spectrum, here of the reference lines from ^{41}Ca and ^{55}Fe and a monochromatic line at 0.525 keV, formed by summing the spectra of the 32 channels after independently correcting the energy scale of each. Early in the calibration program, data were taken at different biases (with the optimal filter regenerated for each one) to determine the bias associated with the best resolution. This determination resulted in the detector being run at a warmer bias temperature than anticipated. In fact, the bias temperature ended up being very nearly the same as that obtained when the

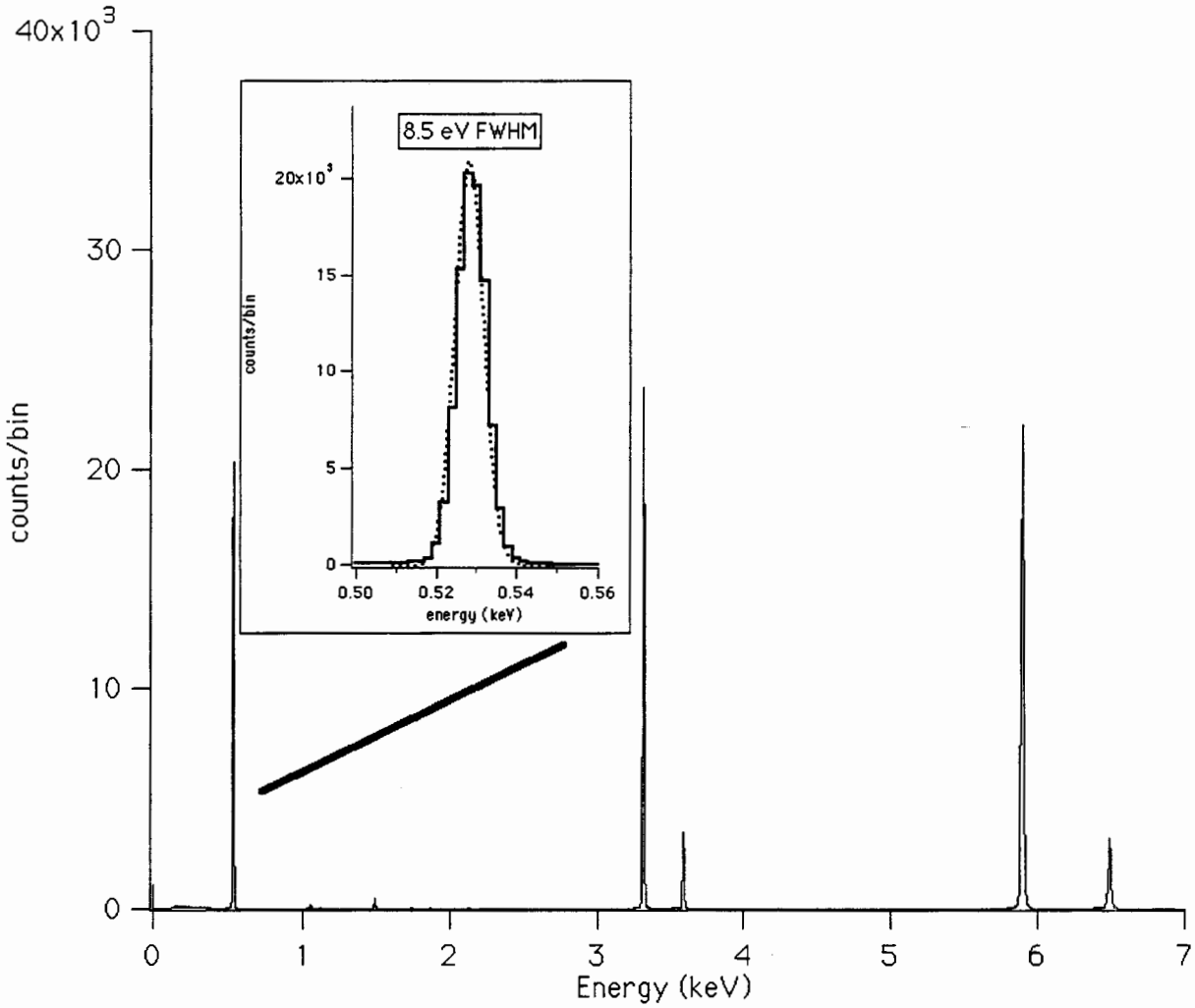

Figure 5. Summed spectrum from 32 XRS pixels after independently gain correcting each one.

detector had been optimally biased with a 65 mK heat sink during laboratory qualification testing. There are advantages to operating with a higher bias, including reducing sensitivity to fluctuations in the heat sink temperature and speeding the pulse recovery time through increasing the magnitude of the electrothermal feedback. At our calibration bias, the exponential fall time of the x-ray pulses was 6 ms. We are still trying to understand the noise spectra measured during this calibration and during subsequent operation of the instrument that led to this choice of a high bias voltage because they are inconsistent with prior noise measurements in the test apparatus. Some of the pixels produced spectral line shapes that had a small high-energy shoulder that increased with incident photon energy. Experiments with partial illumination suggested that this is the manifestation of a dependence of the signal on the site of x-ray absorption. A more detailed discussion of the calibration program and the results of our analysis can be found in Reference 17.

4. THE ANTICOINCIDENCE DETECTOR AND CHARGED PARTICLE REJECTION

Astro-E will be placed into a 550 km, 31° orbit, where the particle background will consist predominantly of protons. The cosmic ray rate seen on the Solid-state Imaging Spectrometer (SIS) instrument on *ASCA* in the same orbit (formerly *Astro-D*, the predecessor of *Astro-E*), was of order 1 count/s/cm^2 of active CCD area.[18] Though this rate also included events induced in the non-active frame-store region of the CCD, we have used 1 count/s/cm^2 as our estimate of the expected proton rate for most of the orbit. Given the expected proton spectrum at that altitude, we expect 4×10^{-3} counts/s/pixel, 63% of which deposit more than 10 keV. Though this would be an acceptable rate, we wanted the extra protection of a particle monitor to allow us to deal with unexpected increases in particle background and to make the acquisition of data during passages of the satellite through the high particle rate region of the orbit known as the South Atlantic Anomaly (SAA) a possibility. An anti-coincidence detector permits us to ascertain confidently whether or not changes in detected flux originate from the astronomical object under observation. It was also desired to have a detector significantly faster than the calorimeters in order to provide diagnostic capability in the event that the calorimeters themselves are saturated.

The XRS anti-coincidence detector is an ionization detector which can operate at the calorimeter heat sink temperature at low (< 9 V) bias. Thus, it can be placed directly behind the calorimeter array. The sensor itself is a very simple design. The chip consists of 1 cm^2 × 0.5 mm of high purity silicon (nominally 13 – 21 kΩ•cm at room temperature). One surface is degenerately doped with phosphorus (n+) while the other is degenerately doped with boron (p+), and both sides are metalized with aluminum. Thus it is configured as a p-i-n diode and is operated with the standard reverse-bias relative to that configuration. The device should not be considered a diode at an operating temperature of ~60 mK, however, because the carriers in the central intrinsic region are completely frozen out and the detector is simply an insulator between metallic contacts. Biases up to 24 V were investigated. No change in gain was seen for biases above 2 V. Below 2 V, the number of anomalous inverted pulses increases. From prior work with operating a p-i-n device at 60 mK, the inverted pulses are probably due to field distortion resulting from localized charges near the edges of the device.[19] The XRS anti-coincidence detector is biased at 6 V by default, but the bias can be commanded from 0 to 8 V.

Though we investigated a number of read-out schemes for the anti-coincidence detector, including conventional charge

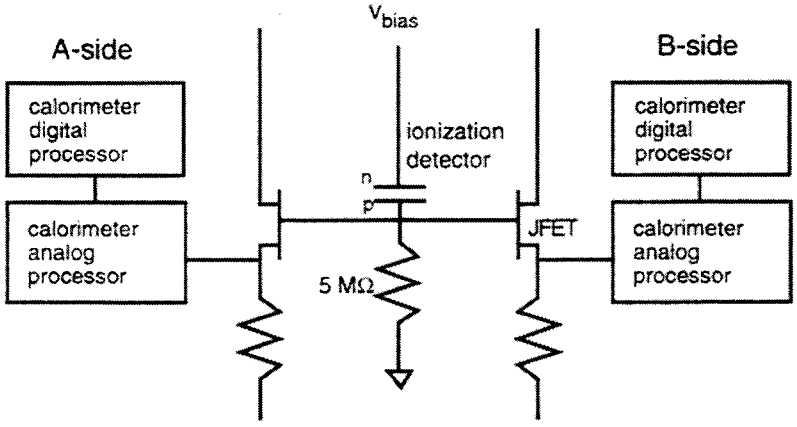

Figure 6. Block diagram of XRS anti-coincidence detector, showing redundancy.

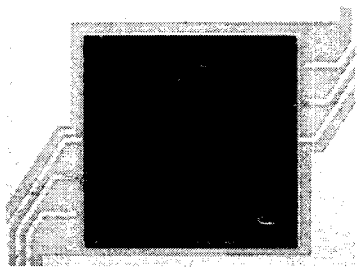

Figure 7. Photograph of anti-coincidence detector.

amplifier circuits, we settled for simplicity on a design identical to the signal amplifier for each calorimeter channel, as shown in Figure 6. The voltage signal due to ionization in the detector appears at the gate of a cold JFET source-follower for impedance shifting and is then amplified by a gain of 20000 before being sent to a comparitor and the anti-coincidence logic. The combined capacitance of the detector and any gate-ground capacitance discharges through 5 MΩ to ground. The advantage to this, in addition to saving engineering time, was avoiding phase lag problems in the use of a large feedback loop from a relatively warm charge amplifier to the cold detector. The disadvantages were the reduction in signal amplitude and the slowing of the recovery time by gate-source capacitance in the JFET and capacitance to ground in the feedthroughs between the detector and the amplifier. This penalty was incurred twice, since the device is wired to separate "A side" and "B side" read-out channels for redundancy. This adds 27 pF to the 21 pF expected for the silicon alone, as determined from the 0.24 ms pulse fall time. The n+ contact was attached to a gold bias contact pad on an alumina board using silver epoxy and the JFET gate connections were made to the top using redundant wire bonds. Figure 7 is a photograph of the mounted detector.

The calorimeter alumina board was placed directly on top of the anti-coincidence detector board, with the anti-coincidence detector itself fitting in a hole in the array board. The top surface of the particle detector sits 0.63 mm below the plane of the calorimeter pixels. About 80% of cosmic rays impacting the calorimeter array will pass through at least 0.5 mm of Si in the anti-coincidence detector. Those that miss will tend to have longer path lengths in the HgTe absorbers, enhancing their rejection based on their being out of the observational band. Some additional discrimination is provided by the calorimeter pulse shape itself. Pulses due to deposition of energy in the HgTe rise more slowly than pulses due to deposition of energy in the silicon thermistor-bearing element. Most cosmic rays deposit energy in both the HgTe and the Si, yielding intermediate rise times. Many of those such events would be rejected as part of the routine calorimeter pulse screening, even without the anti-coincidence flag. This effect came as a pleasant surprise. With 14 μm Si and 8.5 μm HgTe, we expect about 37% of the total energy to be deposited in the Si, not considering the spacer. When we considered this several years ago, our modeling showed that cosmic ray pulses would not be distinguishable from absorber events. Revisiting the modeling, we see that there are several conditions that now work in our favor. We are using thicker Si devices, we have increased the decoupling of the absorber and Si through the use of the spacers, and the use of a lower resistance thermistor increases the difference between

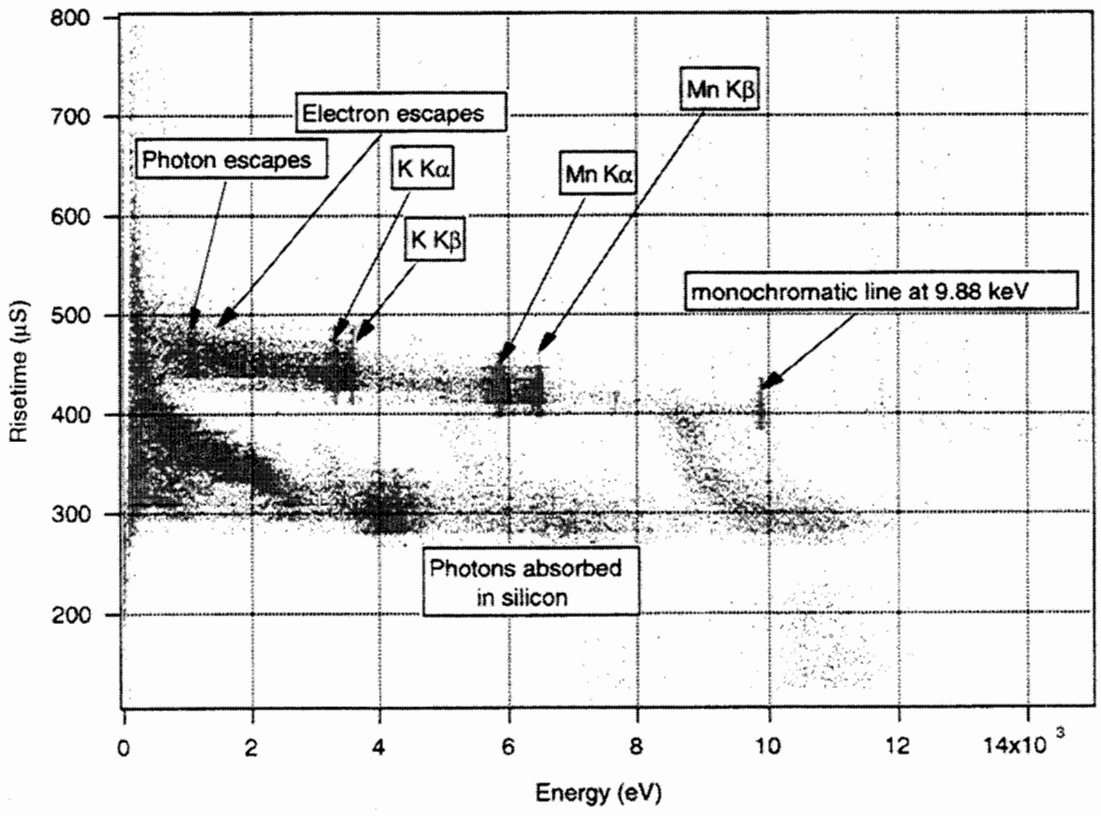

Figure 8. Saturated plot of rise time versus filtered pulse height for XRS calorimeter array.

RC rounded and thermally rounded risetimes. The anti-coincidence flag remains useful, however. The absorbers overhang the Si, so a quarter of the cosmic rays will not have fast rise times, and our rise time discrimination loses sensitivity at the low energy end of the XRS band.

The spectrum of events in the anti-coincidence detector is not recorded on XRS. Calorimeter events that occur within a specified time window of an anti-coincidence event that exceeds a set voltage threshold are telemetered with an anti-coincidence flag. Observers can use or ignore the flag in their analysis. The total rate of anti-coincidence events that exceed the threshold is recorded as part of the housekeeping records. The raw anti-coincidence pulses can be monitored with ground equipment for testing the resolution and the energy scale. Between the point where the pulses are monitored and the discriminator is a filter with a zero at 10 Hz and a pole at 16 kHz, so processing the monitored pulses likewise should permit an estimate of the system resolution. Using the 59.5 keV gamma-rays from an ^{241}Am source, digitizing the pulses, and applying the 16 kHz filter in the pulse height analysis software, we obtain a resolution of 2.7 keV FWHM at 59.5 keV. We expect the spectrum of energy deposited by protons at the anti-coincidence detector to peak at 200 keV, with 99.95% of events depositing > 15 keV. Thus, the geometrical inefficiency is much more limiting than the detector's energy resolution.

The different time scales for detection of energy deposited in the particle detector, in the calorimeter at the HgTe, and in the calorimeter at the Si complicated the definition of coincidence. The anti-coincidence detector pulses rise and peak within the 82 μs calorimeter signal sampling interval. The time stamp assigned to a calorimeter event, however, is tied to the CDP pulse detection algorithm, which is based on the crossing of a threshold by a box-car derivative of the pulse. Because of thermal non-linearity in the calorimeter, there is a trend for pulse risetimes to get shorter for pulses of increasing energy, as illustrated in Figure 8. On top of this, for a given energy, energy deposited in the silicon causes a faster response than energy deposited in the HgTe. Accounting for the group delay of the anti-aliasing filter on the calorimeter pulses, coincidence had to be defined as $-11 < \Delta \leq -6$, for $\Delta = (t_{anti\text{-}co} - t_{calorimeter})/t_{samp}$ where t_{samp} = 82 μs, in order to cover the full range of calorimeter pulse shapes. If the rate of false coincidences becomes a problem with this size window, the range could be changed to $-11 < \Delta \leq -8$. Most events resulting from cosmic rays depositing energy in the silicon of the calorimeters would not get flagged, but data cleaning should discard events with such rise times anyway. High energy (> 20 keV) cosmic ray events in the HgTe also would not be flagged.

The impact of false coincidence depends entirely on the rate of triggers at the particle counter. With the 5-sample-wide window and a rate of 1 count/s at the anti-coincidence detector, the probability that a valid x-ray photon will be flagged as a particle event is 4.1×10^{-4}, an acceptable rate. If the rate is 1000 counts/s, such as on passage through the SAA, then 34% of all valid photon events will be mislabeled as particle events. (Of course, the ability to take data during SAA passages will depend on several other factors, such as induced photon background, thermal loading of the calorimeter mount, and electronic upsets.) Since the probability of false flagging is the same for any event, it results in an energy-independent correction to the observation efficiency. Since the anti-coincidence rate is monitored, this is an easy correction to make, and outweighs the uncertainty of leaving real cosmic proton events in the source spectrum. The spectrum of "anti"-flagged events can be compared to the cleaned spectrum as a diagnostic.

5. CONCLUSION

XRS will be the first microcalorimeter spectrometer in orbit and will inaugurate a new age of high-resolution, high throughput astrophysical spectroscopy. We anxiously await the first in-orbit data!

ACKNOWLEDGMENTS

We thank M. Bevan and H.-D. Shih of Texas Instruments for their dedication in developing and delivering the HgTe absorbers for XRS. We also extend heartfelt thanks to C. Sappington and F. Peters for their help and expertise in unconventional wirebonding and dicing situations. We gratefully recognize the work of C. Fechtmann in testing the evolving anti-coincidence detector design while a visiting summer student.

REFERENCES

1. R. L. Kelley, K. R. Boyce, S. R. Breon, S. S. Holt, S. H. Moseley, Jr., D. B. Mott, F. S. Porter, C. K. Stahle, A. E. Szymkowiak, M. D. Audley, K. C. Gendreau, R. Fujimoto, K. Mitsuda, Y. Ishisaki, D. McCammon, and T. Mihara, "*Astro-E* High-resolution X-ray Spectrometer", *Proc. SPIE*, **3765**, this volume.
2. Y. Ogawara, "The *Astro-E* mission", *IAU Symposium*, **188**, pp. 75-78, 1998.
3. K. R. Boyce, R. G. Baker, J. J. Dumonthier, R. L. Kelley, C. K. Stahle, A. E. Szymkowiak, G. E. Winkert, M. D. Audley, K. C. Gendreau, R. Fujimoto, and Y. Ishisaki, "Design and Performance of the *Astro-E*/XRS Signal Processing System", *Proc. SPIE*, **3765**, this volume.
4. A. E. Szymkowiak, R. L. Kelley, S. H. Moseley, and C. K. Stahle., "Signal Processing for Microcalorimeters", *J. Low Temp. Phys.*, **93**, pp. 281-285 ,1993.
5. D. B. Mott, S. B. Dutta, R. McClanahan, R. P. Brekosky, C. M. Stahle, R. L. Kelley, C. K. Stahle, and A. E. Szymkowiak, "Fabrication of Monolithic Silicon Calorimeters", *Proc. Seventh Int. Workshop on Low Temperature Detectors*, pp. 119-120, 1997.
6. C. K. Stahle, R.P. Brekosky, S.B. Dutta, K.C. Gendreau, R.L. Kelley, R.A. McClanahan, D. McCammon, S.H. Moseley, D.B. Mott, F.S. Porter, and A.E. Szymkowiak "The Physics and the Optimization of the XRS Calorimeters on *Astro-E*", to appear in *Nucl. Instr. and Meth.*, 1999.
7. C. K. Stahle, R. L. Kelley, S. H. Moseley, A. E. Szymkowiak, M. Juda, D. McCammon, and J. Zhang, "Thermalization of X-rays in Evaporated Tin and Bismuth Films Used as the Absorbing Materials in X-ray Calorimeters", *J. Low Temp. Phys.*, **93**, pp. 257-262, 1993.
8. C. K. Stahle, R. L. Kelley, D. McCammon, S. H. Moseley, and A. E. Szymkowiak, "Microcalorimeter Arrays for High Resolution Soft X-ray Spectroscopy", *Nucl. Instr. and Meth.* **A370**, pp. 173-176, 1996
9. A. L. Efros, "Coulomb Gap in Disordered Systems", *J. Phys. C*, **9**, pp. 2021-2030, 1976.
10. J. Zhang, W. Cui, M. Juda, D. McCammon, R.L. Kelley, S.H. Moseley, C.K. Stahle, and A.E. Szymkowiak, "Hopping Conduction in Partially Compsenated Doped Silicon", *Phys. Rev. B*, **48**, pp. 2312-2319, 1993.
11. S.-I. Han, R. Almy, E. Apodaca, W. Bergmann, S. Deiker, A. Lesser, D. McCammon, K. Rawlins, R.L. Kelley, S.H. Moseley, F.S. Porter, C.K. Stahle, and A.E. Szymkowiak, "Instinsic 1/f Noise in Doped Silicon Thermistors for Cryogenic Calorimeters", *Proc. SPIE*, **3445**, pp. 640-644 , 1998.
12. J. Zhang, W. Cui, M. Juda, D. McCammon, R.L. Kelley, S.H. Moseley, C.K. Stahle, and A.E. Szymkowiak, "Non-ohmic Effects in Hopping Conduction in Doped Silicon and Germanium Between 0.05 and 1 K", *Phys. Rev. B*, **57**, pp. 4472-4481, 1998.
13. F. S. Porter, M. J. DiPirro, R. L. Kelley, T. Pham, C. K. Stahle, A. E. Szymkowiak, J. G. Tuttle, M. D. Audley, K. C. Gendreau, R. P. Brekosky, J. D. Gygax, D. McCammon, R. J. Paulos, and S. D. Murphy "Detector Assembly and the Ultralow-temperature Refrigerator for XRS", *Proc. SPIE*, **3765**, this volume.
14. S. H. Moseley, J.C. Mather and D. McCammon, "Thermal Detectors as X-ray Spectrometers", *J Appl. Phys.* **56**, pp. 1257-1262, 1984.
15. J. C. Mather, "Bolometer Noise: Nonequilibrium Theory", *Appl. Optics*, **21**, pp. 1125-1129, 1982.
16. P. M. Downey, A. D. Jeffries, S. S. Meyer, R. Weiss, F. J. Bachner, J. P. Donnelly, W. T. Lindley, R.W. Mountain, and D. J. Silversmith, "Monolithic Silicon Bolometers", *Appl. Optics*, **23**, pp. 910-914, 1984.
17. K. C. Gendreau, M. D. Audley, K. A. Arnaud, K. R. Boyce, R. L. Kelley, F. S. Porter, C. K. Stahle, A. E. Szymkowiak, R. Fujimoto, K. Mitsuda, Y. Ishisaki, and T. Mihara, "*Astro-E*/XRS Calibration Program and Results", *Proc. SPIE*, **3765**, this volume.
18. K. C. Gendreau, "X-ray CCDs for Space Applications: Calibration, Radiation Hardness, and Use for Measuring the Spectrum of the Cosmic X-ray Background", Ph.D. thesis, Massachusetts Institute of Technology, 1995.
19. C. K. Stahle, J. Wouters, R. L. Kelley, S. H. Moseley, and A. E. Szymkowiak, "Charge Collection and Thermalization in a Composite Calorimetric and Ionization Detector", *J. Appl. Phys.*, **75**, pp. 3723-3731, 1994.